Karakoç, Alp; Paltakari, Jouni; Taciroglu, Ertugrul

Data-Driven Computational Homogenization Method Based on Euclidean Bipartite Matching

Published in:
Journal of Engineering Mechanics

DOI:
10.1061/(ASCE)EM.1943-7889.0001708

Published: 01/02/2020

Document Version
Peer-reviewed accepted author manuscript, also known as Final accepted manuscript or Post-print

Please cite the original version:
Karakoç, A., Paltakari, J., & Taciroglu, E. (2020). Data-Driven Computational Homogenization Method Based on Euclidean Bipartite Matching. *Journal of Engineering Mechanics*, *146*(2), Article 04019132. https://doi.org/10.1061/(ASCE)EM.1943-7889.0001708

A DATA-DRIVEN COMPUTATIONAL HOMOGENIZATION METHOD BASED ON EUCLIDEAN BIPARTITE MATCHING

Alp Karakoç[1], Jouni Paltakari[2], Ertugrul Taciroglu[3]

[1]Postdoctoral researcher, Civil & Env. Engineering Department, University of California Los Angeles, 90095 CA, USA. Email: akarakoc@alumni.ucla.edu

[2] Professor, Aalto University, Department of Bioproducts and Biosystems, FI-00076 AALTO, FINLAND. Email: jouni.paltakari@aalto.fi

[2] Civil & Env. Engineering Department, University of California Los Angeles, 90095 CA, USA. Email: etacir@ucla.edu

ABSTRACT

Image processing methods combined with scanning techniques—e.g., microscopy or micro-tomography—are now being frequently used for constructing realistic microstructure models that can be used as representative volume elements (RVEs) to better characterize heterogeneous material behavior. As a complement to those efforts, the present study introduces a computational homogenization method that bridges the RVE and material-scale properties in situ. To define the boundary conditions properly, an assignment problem is solved using Euclidean bipartite matching through which the boundary nodes of the RVE are matched with the control nodes of the rectangular prism bounding the RVE. The objective is to minimize the distances between the control and boundary nodes, which when achieved enables the bridging of scale-based features of both virtually generated and image-reconstructed domains. Following the minimization process, periodic boundary conditions can be enforced at the control nodes, and the resulting boundary value problem can be solved to determine the local constitutive material behavior. To verify the proposed method, virtually generated domains of closed-cell porous, spherical particle and fiber reinforced composite materials are analyzed, and the results are compared with analytical Hashin-Shtrikman and Halpin-Tsai methods. The percent errors are within the ranges from 0.04% to 3.3%, from 2.7% to 14.9%, and from 0.5% to 13.2% for porous, particle and fiber reinforced composite materials, respectively, indicating that the method has a promising potential in the fields of image-based material characterization and computational homogenization.

KEYWORDS: Microscopy, micro-tomography, representative volume element, assignment problem, material characterization, computational homogenization.

INTRODUCTION

Image processing methods combined with scanning techniques—e.g., laser scanning confocal microscopy, micro-computed tomography (μCT), scanning electron microscopy (SEM), magnetic resonance imaging (MRI) to name a few—are gaining attention due to their capabilities in determining surface and volumetric properties, chemical compositions, and mechanical and directional features of materials (Nazar et al. 1996; Huang and Wei 2010; Duval et al. 2014). Although there are various complexities in image acquisition, segmentation and rendering and needs for considerable user interaction, these methods have been paving the way to highly refined levels of data-driven material characterization (Hollister and Kikuchi 1994; Terada et al. 1997). In addition to the innovations and developments in the image acquisition systems, numerous segmentation and rendering techniques have been also developed to process the obtained image data and extract high-fidelity models (Takano et al. 2003; Legrain et al. 2011; Lopez et al. 2014; Ren et al. 2015). In most of these techniques, the solution domain is discretized with the aim of minimum data loss to reconstruct so-called realistic representative volume element (RVE), to which the mechanical and physical properties, and boundary conditions are assigned (Lian et al. 2013; Bargmann et al. 2018). Boundary volume problem (BVP) can be then solved—e.g., using the finite element method in the computational homogenization framework— over the RVE boundaries to bridge the micro- and material-scale properties for the effective mechanical properties (Geers et al. 2010; Karakoc et al. 2017). However, due to unstructured nature of the reconstructed RVEs directly from the images, defining the RVE boundaries and node mapping for computational homogenization—especially, in the case of periodic boundary definitions— can turn into a nontrivial process (Lian et al. 2013; Nguyen and Noels 2014). To the authors' knowledge, various boundary condition enforcement methods are available in the literature including the local implementation method (Tyrus et al. 2007), master/slave approach (Yuan and Fish 2008), weak periodicity (Larsson et al. 2011). Most of these methods have been successfully tested on RVEs composed of inclusions embedded in matrix; however, there still needs to be development in enforcement methods—e.g., in case of the dominant presence of pores on the RVE boundaries (see, Figure 1) (Nguyen et al. 2012).

In consideration to the challenges in data-driven material characterization, the present study introduces a computational homogenization method, through which periodic boundary conditions are enforced via total distance minimization of control and boundary node sets as shown in Figure 2. This, in turn, enables computational homogenization of domains represented by arbitrary meshes—e.g., in-situ reconstructed domains via image processing methods, and bridging of scale-based features of both image-reconstructed and virtually generated domains. The present study is therefore expected to advance the current state of the art towards accurate material characterization with low computational costs.

METHODOLOGY

As illustrated in Figures 2 and 3, the BVP is defined at the RVE scale first wherein the boundary nodes (p) on the RVE boundaries ($\partial\omega$) are matched with the control nodes (q), which are uniformly discretized and represented in the form of corner, edge, and surface nodes on the boundaries ($\partial\Gamma$) of its bounding rectangular prism. The grid spacing on $\partial\Gamma$, is taken as the mean value d_{mean} of the closest-pair distances on the corresponding $\partial\omega$ surface. Simply, the closest-pair distance is calculated as the Euclidean distance between the reference p node and its nearest neighbor. After this step, alpha shapes method is used to reduce the q set size. Thereafter, one-to-one matching between p and q sets are carried out through a distance minimization technique known as the Euclidean bipartite matching. Eventually, periodic boundary conditions are enforced, rigid body rotations are eliminated, and the BVP is solved in the computational homogenization scheme based on the first-order strain-driven homogenization method.

Control node reduction

In order to reduce the excessive amount of control nodes—i.e., q node set size reduction, especially for the RVE boundaries with pores, the alpha shapes method is used (Edelsbrunner et al. 1983; Edelsbrunner 1995). As illustrated in Figure 4, the boundary nodes p obtained from the geometry file is used to construct (I) control node sets as grid points by means of d_{mean} and (II) Delaunay triangulation where the elements (polygons in 2D and polyhedrons in 3D), the circumradii R of which exceeds the alpha shape value (taken to be d_{mean} in the present study), are discarded (Cerquaglia et al. 2017). Thereafter, the control nodes are refined by eliminating the control nodes in the region of excessive elements identified with the alpha shapes method.

Euclidean bipartite matching of the boundary and control nodes

The core of the proposed method is based on Euclidean bipartite matching of the boundary nodes denoted with p and with q, as depicted in Figure 2. The total distance between the node sets are minimized to determine an optimal matching and thus, to obtain one-to-one correspondence between p and q. As the first step, a cost matrix based on the Euclidean distance of each (p, q) combination is generated, which results to an $N \times N$ matrix where N is equal to the set length of p—i.e.,

$$\begin{bmatrix} \mathbf{d}(p_1,q_1) & \mathbf{d}(p_1,q_2) & \cdots & \mathbf{d}(p_1,q_n) \\ \mathbf{d}(p_2,q_1) & \cdots & \cdots & \cdots \\ \cdots & \cdots & \cdots & \cdots \\ \mathbf{d}(p_n,q_1) & \cdots & \cdots & \mathbf{d}(p_n,q_n) \end{bmatrix}. \tag{1}$$

Then, optimal permutation of matched nodes is discerned based on their total Euclidean distances through the minimization problem

$$T = \min \sum_{\Pi} \mathbf{d}(p,q) \tag{2}$$

where $\mathbf{d}$ is the Euclidean distance function for two nodes, T is the total Euclidean distance and Π is the permutations that abide a one-to-one correspondence. Under these circumstances, there should be only one matching pair for each p and q, otherwise the one-to-one correspondence condition is violated. The problem in Eq. (2) can be solved with—e.g., Monte-Carlo simulations generating random possible solutions and selecting the solution with the minimum cost, various heuristics for determining the optimum cost, or schemes relaxing the given problem into a series of problems for each of which an optimal solution is obtained (Rendl 1988; Hung and Rom 1980; Karakoc and Taciroglu 2017). In the present study, Monte Carlo simulations are used, for which the solution provides one-to-one matching of control and boundary nodes that exhibit the shortest total distance T, as shown in Figure 2. Following the matching process, there are two possible options in defining the boundary conditions: (*i*) to use directly the boundary nodes p obtained as a result of the minimization, or (*ii*) further, to tie the degrees of freedom of the one-to-one matched nodes and to use the control nodes q (—i.e., $\vec{u}_p = \vec{u}_q$). In the present study, the latter option is preferred.

First-order computational homogenization

In the present study, a first-order strain driven homogenization is utilized to determine the elastic properties. As shown in Figure 5, the macro-strain $\mathbf{e}^{\mathrm{M}}$ is known *a priori* where the associated macro-stress $\mathbf{s}^{\mathrm{M}}$ is computed through volume averaging of the stress field at the RVE scale (Hernández et al. 2014).

Here, the macro-strain e_{ij}^{M} for $i, j \in \{X, Y, Z\}$ is the given parameter and is used as the driving parameter of the microscopic displacement field for the RVE so that

$$\vec{u}^{\mathrm{m}} = \vec{r} \cdot \mathbf{e}^{\mathrm{M}} + \underline{\vec{u}}. \quad (3)$$

The first addend of Eq. (3) on the right-hand side represents the macroscopic displacement contribution, and the second represents the displacement fluctuation field $\underline{\vec{u}}$ due to heterogeneities within the RVE (Geers et al. 2010). Here, $\vec{r}$ represents the position vector between two nodes and the overall body is assumed to be composed of repeating rectangular prism bounding the RVEs. Continuity conditions for the displacement field are satisfied at each adjacent boundary by taking the relative positions of the control node sets q, which eliminates $\underline{\vec{u}}$.

In computational homogenization studies, the use of RVEs with periodic boundary conditions is a common practice, for which the corresponding corner, edge and surface nodes are matched as previously depicted in Figure 3, and suffices to represent the effective material deformation (Karakoc 2018). Following this common practice, periodic boundary conditions are applied onto the control nodes q of the rectangular prism bounding the RVE. Here, it is important that the so-called “periodic offset” caused by the distance between matched nodes is inevitable.

Hill-Mandel principle and stress averaging

In computational homogenization, Hill-Mandel principle gives the relationship between the micro- and material scales such that

$$\mathbf{s}^{\mathrm{M}} : \mathbf{e}^{\mathrm{M}} = \frac{1}{\Gamma} \int_{\Gamma} \mathbf{s}^{\mathrm{m}} : \mathbf{e}^{\mathrm{m}} \, \mathrm{d}\Gamma , \tag{4}$$

for which superscripts m and M stand for micro- and material scales. The symbol (:) denotes the inner product $\mathbf{a} : \mathbf{b} = a_{ij} b_{ij}$ for second-order tensors. By using the Gauss theorem, Eq. (4) can be rewritten over $\partial\Gamma$ as

$$\mathbf{s}^{\mathrm{M}} : \mathbf{e}^{\mathrm{M}} = \frac{1}{\Gamma} \int_{\partial\Gamma} \vec{t}^{\,\mathrm{m}} \cdot \vec{u}^{\,\mathrm{m}} \, \mathrm{d}\partial\Gamma , \tag{5}$$

where $\vec{t}^{\,\mathrm{m}}$ is the micro-scale traction vector at $\partial\Gamma$. By plugging the boundary periodicity into Eq. (5), we get

$$\mathbf{s}^{\mathrm{M}} : \mathbf{e}^{\mathrm{M}} = \frac{1}{\Gamma} \int_{\partial\Gamma} \vec{t}^{\,\mathrm{m}} \cdot \left(\vec{r} \cdot \mathbf{e}^{\mathrm{M}} \right) \mathrm{d}\partial\Gamma + \frac{1}{\Gamma} \int_{\partial\Gamma} \vec{t}^{\,\mathrm{m}} \cdot \underline{\vec{u}} \, \mathrm{d}\partial\Gamma , \tag{6}$$

which can be rearranged into

$$\mathbf{s}^{\mathrm{M}} : \mathbf{e}^{\mathrm{M}} = \frac{1}{\Gamma} \int_{\partial\Gamma} \left(\vec{t}^{\,\mathrm{m}} \otimes \vec{r} \right) \mathrm{d}\partial\Gamma : \mathbf{e}^{\mathrm{M}} + \frac{1}{\Gamma} \int_{\partial\Gamma} \vec{t}^{\,\mathrm{m}} \cdot \underline{\vec{u}} \, \mathrm{d}\partial\Gamma . \tag{7}$$

Here, the symbol $\otimes$ denotes the dyadic operator. The second integrand at the right-hand side vanishes in case of periodic boundary conditions. Hence, macro-scale stress $\mathbf{s}^{\mathrm{M}}$ can be expressed as the volume average of the micro-scale stress $\mathbf{s}^{\mathrm{m}}$ such that

$$\mathbf{s}^{\mathrm{M}} = \frac{1}{\Gamma} \int_{\partial\Gamma} \left(\vec{t}^{\,\mathrm{m}} \otimes \vec{r} \right) \mathrm{d}\partial\Gamma = \frac{1}{\Gamma} \int_{\Gamma} \mathbf{s}^{\mathrm{m}} \, \mathrm{d}\Gamma , \tag{8}$$

where Γ is the total volume of the rectangular prism bounding the RVE. Then, the given strains $\mathbf{e}^{\mathrm{M}}$ and the computed stresses $\mathbf{s}^{\mathrm{M}}$ at the material scale can be then combined. Eventually, by means of a least-squares minimization of all six distinct deformation modes in three-dimensional space (three axial and three shear loading modes), the compliance $\mathbf{C}^{\mathrm{M}}$ is obtained as

$$\pi(C_{11}, .., C_{66}) = \sum_{i=1}^{n} \left\| \mathbf{e}_i^{\mathrm{M}} - \mathbf{C}^{\mathrm{M}} : \mathbf{s}_i^{\mathrm{M}} \right\|^2 , \tag{9}$$

where *i* refers to the number of experiments (Karakoç et al. 2013; Sjolund et al. 2014).

CONVERGENCE

In order to understand the capability of the algorithm, effect of RVE mesh size and control node number on the convergence of effective elastic properties and central processing unit (CPU) time study are investigated. For this purpose, the closed cell porous RVEs, which can be sometimes computationally expensive due to the non-proportional number of pores in the opposing surfaces, have been generated. The matrix material is selected to be epoxy resin with $E_m = 3000$ MPa and $v_m = 0.38$. Two sets of simulations have been carried out: (I) one set of simulations with different number of seeds per edge s={2, 2.2, 2.5, 2.9, 3.3, 4, 5, 6.7, 10, 20, 40} and corresponding mesh sizes e={46768, 49178, 50782, 53388, 57556, 68388, 69961, 86193, 102843, 185795, 558311}, three RVEs of which are depicted in Figure 6a, and (II) one set of simulations with different control node numbers q={152, 568, 1224, 2402, 2906, 3458, 3628}, three RVEs of which are shown in Figure 7a.

As seen in Figure 6b, there is a positive correlation between the mesh size and CPU time. Despite this trade-off, the effective elastic properties do not vary with increasing mesh size—e.g., after RVE with 185795 elements referring to edge seeding number of 20. Even though the element size in the finest RVE mesh is almost triple reaching 558311 elements, the maximum percentile difference is low and obtained as 3.8 % for E_{33}. However, there is extreme increase in the CPU time from 423 seconds to 1992 seconds for these two cases. Based on the results, element size is based on the edge seeding number of 20 in the present study. Thereafter, the effect of control node number on the effective elastic properties and CPU time have been investigated. The RVE is selected to be the one with 185795 elements—i.e, edge seeding number of 20. As seen in Figure 7b, there is a fast convergence for both the effective elastic properties and CPU time with a maximum value of 423 seconds showing that the present framework works efficiently with even moderate numbers of control nodes.

METHOD VERIFICATION

Previously conducted analytical, numerical and experimental studies and their results on closed cell porous materials, particle and fiber reinforced composites, the microstructures of which are illustrated in Figure 1, are used so as to verify the present method (Hashin and Shtrikman 1963; Halpin 1969; Kushnevsky et al. 1998; Segurado and Llorca 2002; Babu et al. 2018).

Case study: Closed cell porous and spherical particle reinforced composites

In order to verify the present method for closed cell porous and spherical particle reinforced composites, RVE geometries are formed based on the procedure provided by Segurado and Llorca (Segurado and Llorca 2002). In line with this procedure, two cases are considered, for which unit cubes ($1\times1\times1$) containing 30 non-overlapping randomly distributed reinforcing particles and voids are generated with an in-house random sequential adsorption (RSA) code (Evans 1993). In this code, if the particles or voids do not overlap with the previous ones, they remain fixed till the end of the computational process reaching the desired particle or void volume fractions $V_{\mathrm{f}} = \left(\sum_{i=1}^{30} 4/3\pi r_i^3 \right)$ of the RVEs. In this case study, V_{f} is taken to be within the range from 10% to 28%. The generated RVE domains are then discretized by using C3D4 general-purpose tetrahedral elements of ABAQUS (Hibbitt et al. 1992). The matrix material is selected to be epoxy resin with $E_{\mathrm{m}} = 3000$ MPa and $v_{\mathrm{m}} = 0.38$ and the reinforcing particles are chosen to be glass with $E_{\mathrm{f}} = 70000$ MPa and $v_{\mathrm{f}} = 0.20$ in case of particle reinforced composites. In case of voids, E_{f} is taken to be arbitrarily small (—i.e., ~ 0 Pa). Due to heterogeneities in the RVEs, three numerical simulations are conducted with the ABAQUS Standard finite element solver for each case and the simulation results are compared with the analytical Hashin-Shtrikman bounds for both the closed cell porous materials and the particle reinforced composites. Under the assumption of linear elastic isotropic phases, these bounds for bulk K and shear G moduli are given as (Hashin and Shtrikman 1963; Kushnevsky et al. 1998)

$$K_{\mathrm{c}}^{\mathrm{u}} = K_{\mathrm{f}} + \frac{\left(K_{\mathrm{m}} - K_{\mathrm{f}}\right)\left(3K_{\mathrm{f}} + 4G_{\mathrm{f}}\right)\left(1 - V_{\mathrm{f}}\right)}{\left(3K_{\mathrm{f}} + 4G_{\mathrm{f}}\right) + 3\left(K_{\mathrm{m}} - K_{\mathrm{f}}\right)V_{\mathrm{f}}}, \tag{10}$$

$$K_{\mathrm{c}}^{\mathrm{l}} = K_{\mathrm{m}} + \frac{\left(K_{\mathrm{f}} - K_{\mathrm{m}}\right)\left(3K_{\mathrm{m}} + 4G_{\mathrm{m}}\right)V_{\mathrm{f}}}{\left(3K_{\mathrm{m}} + 4G_{\mathrm{m}}\right) + 3\left(K_{\mathrm{f}} - K_{\mathrm{m}}\right)\left(1 - V_{\mathrm{f}}\right)}, \tag{11}$$

$$G_{\mathrm{c}}^{\mathrm{u}} = G_{\mathrm{f}} + \frac{5G_{\mathrm{f}}\left(G_{\mathrm{m}} - G_{\mathrm{f}}\right)\left(3K_{\mathrm{f}} + 4G_{\mathrm{f}}\right)\left(1 - V_{\mathrm{f}}\right)}{5G_{\mathrm{f}}\left(3K_{\mathrm{f}} + 4G_{\mathrm{f}}\right) + 6\left(G_{\mathrm{m}} - G_{\mathrm{f}}\right)\left(K_{\mathrm{f}} + 2G_{\mathrm{f}}\right)V_{\mathrm{f}}}, \tag{12}$$

$$G_{\mathrm{c}}^{\mathrm{l}} = G_{\mathrm{m}} + \frac{5G_{\mathrm{m}}\left(G_{\mathrm{p}} - G_{\mathrm{m}}\right)\left(3K_{\mathrm{m}} + 4G_{\mathrm{m}}\right)V_{\mathrm{f}}}{5G_{\mathrm{m}}\left(3K_{\mathrm{m}} + 4G_{\mathrm{m}}\right) + 6\left(G_{\mathrm{f}} - G_{\mathrm{m}}\right)\left(K_{\mathrm{m}} + 2G_{\mathrm{m}}\right)\left(1 - V_{\mathrm{f}}\right)}. \tag{13}$$

Here, the superscripts u and l denote the upper and lower bounds whereas subscripts c, f, and m refer to composite, filling (particle or void), and matrix materials, respectively. The effective Young's modulus, Poisson's ratio and shear modulus values of the composite are then expressed as $E_{c11}=E_{c22}=E_{c33}=9K_cG_c/(3K_c+G_c)$, $\nu_{c12}=\nu_{c13}=\nu_{c23}=(3K_c-2G_c)/(2(3K_c+G_c))$, $G_{c12}=G_{c13}=G_{c23}=G_c$, respectively.

Effective elastic properties of closed cell porous materials

Void presence in materials is generally undesired and can drastically degrade the stiffness and strength properties. Therefore, to understand the effect of voids on the effective elastic properties of closed cell porous materials, all six distinct loading modes are simulated as seen in Figure 8. The least-squares minimization problem of Eq. (9) is then solved to obtain the compliance,—hence E_{c11}, E_{c22}, E_{c33}, G_{c12}, G_{c13}, G_{c23}, and ν_{c12}, ν_{c13}, ν_{c23}.

Both the proposed method and the analytical solution show that there is a negative influence of voids on the elastic properties with a decrease of 28-29% for Young's moduli, 27% for shear moduli and 5% for Poisson's ratios within the investigated volume fraction range, as listed in Table 1. The percent errors for Young's moduli, shear moduli, and Poisson's ratios between the proposed and analytical solutions are 0.04% - 2.9%, 0.1% - 2.5%, 0.1% - 3.3%, respectively.

Effective elastic properties of spherical particle reinforced composites

For the particle reinforced composite simulations, particles and matrix are assumed to be strongly bonded and only the effects of particle volume fraction on the effective elastic properties are examined. In order to deviate from the conventional computational homogenization methods, the domain is discretized so that arbitrary meshes are generated on the RVE boundaries $\partial\omega$, as illustrated in Figure 9. Both uniaxial and shear deformation modes are simulated to obtain the effective elastic parameters listed in Table 2.

The results show the reinforcing effect of particles on the elastic properties with an increase of 67-69% for Young's moduli, 65-66% for shear moduli, and a decrease of 8-13% for Poisson's ratios within the investigated volume fraction range. The decrease in v is due to $v_{\mathrm{f}} < v_{\mathrm{m}}$. The percent errors for Young's moduli, shear moduli, and Poisson's ratios between the proposed and analytical solutions are 3.0%-17.6%, 2.7%-15.3%, 11.2%-14.9%, respectively.

Case study: Fiber reinforced composites

For the verification purpose of the model for the fiber reinforced composites, Halpin-Tsai equations, which were empirically developed to determine the effective elastic properties of aligned fiber composites, are used (Halpin 1969). These equations can be expressed as

$$\frac{\phi_{\mathrm{c}}}{\phi_{\mathrm{m}}} = \frac{1+\xi\eta V_{\mathrm{f}}}{1-\eta V_{\mathrm{f}}}, \tag{14}$$

$$\eta = \frac{\phi_{\mathrm{f}}/\phi_m - 1}{\phi_{\mathrm{f}}/\phi_m + \xi}, \tag{15}$$

for which the aspect ratio is $\xi = 2\times\left(l_{\mathrm{f}}/d_{\mathrm{f}}\right)$ with l_{f} being the fiber length and d_{f} being the fiber diameter. In Equations (14) and (15), ϕ_{c}, ϕ_{m}, ϕ_{f} refer to composite, matrix and fiber elastic material properties, and V_{f} is the volume fraction. Following the investigations in the literature, V_{f} is taken to be within the range from 16% to 33% while AS4 carbon fibre is used as the fiber reinforcement with $E_{\mathrm{f}11}$=225000 MPa, $E_{\mathrm{f}22}$=15000 MPa, $G_{\mathrm{f}12}$=15000 MPa, $G_{\mathrm{f}12}$=7000 MPa, $v_{\mathrm{f}12}$=0.2, and the matrix material is 3501-6 epoxy matrix material with E_{m}=4200 MPa, G_{m}=1567 MPa and v_{m}=0.35 (Soden et al. 1998; Babu et al. 2018). The RVEs are rectangular prisms ($7\times7\times4$) and the fiber aspect ratio ξ=3.5 where both matrix and fiber domains are discretized with C3D4 general-purpose tetrahedral elements.

Effective elastic properties of fiber reinforced composites

In this case study, unidirectionally aligned fiber reinforced composite RVEs are generated with RSA code similar to the previous case study. These RVEs are then investigated and their effective elastic properties are computed. The fibers and matrix are assumed to be strongly bonded and only the effects of fiber volume fraction on the effective elastic properties are examined. The domain is discretized so that arbitrary meshes are generated on the RVE boundaries $\partial\omega$, as seen in Figure 10. Thereafter, six different deformation modes—three uniaxial and shear deformation modes—are simulated to obtain all the effective elastic parameters that are listed in Table 3. The results show that there is a reinforcing effect of fibers on the elastic properties with a steep increase of 125% for E_{c11}, 27% for E_{c22}, and 29% for E_{c33}; 38% for G_{c12}, 45% for G_{c13}, and 26% for G_{c23}; and a decrease of 6% for v_{c12}, 10% for v_{c13}, and 3% for v_{c23} within the investigated volume fraction range. The decrease in v is also experienced with increasing V_f in this case study due to $v_f < v_m$. The percent errors for Young's moduli, shear moduli, and Poisson's ratios between the proposed and analytical solutions are 4.4%-13%, 0.5%-13.2%, 0.5%-5.1%, respectively.

CONCLUSIONS

In the present study, a data-driven computational homogenization method is presented, the objective of which is to characterize effective material properties directly through their reconstructed microstructures via scanning devices (—e.g., X-ray micro-tomography, etc.). For this purpose, periodic boundary conditions are enforced on the reconstructed microstructures via total distance minimization of control and boundary node sets. Here, the minimization problem, here also referred as Euclidean bipartite matching, is solved with Monte-Carlo simulations which generate random possible solutions and select the solution with the minimum cost. This results in one-to-one matching between the node sets. Thereafter, first order strain driven homogenization is implemented, which, in turn, enables bridging scale-based features and material characterization. In order to understand the performance of the method, first, a convergence study has been conducted on porous RVEs that have non-conformal meshes on their boundaries. It is deduced that the increase in the mesh size after some threshold does not have any significant effect —e.g., the maximum percentile difference of 3.8 % between 185795 (referring to 20 seeds per edge) and 558311 elements (40 seeds per edge) despite the tremendous increase in time from 423 seconds to 1992 seconds. Thus, in the present study, 20 seeds per edge is also used in the method verification process. To elaborate, the method is verified by comparing the numerical results computed for realistic renderings of closed cell porous, particle and fiber reinforced composite materials with analytical Hashin-Shtrikman and Halpin-Tsai methods. The percent errors between the analytical and computed effective elastic properties are observed to be within acceptable ranges—namely, 0.04%-3.3% for porous material case, 2.7%-17.6% for particle reinforced composite material case, and 0.5%-13.2% for fiber reinforced composite material case. These results indicate that the proposed data-driven computational homogenization method is a potentially useful tool that can utilize in-situ imaging data at the micro-scale as input, and produce effective properties at the material (meso-) scale.

ACKNOWLEDGMENTS

The authors gratefully acknowledge the support of Tekniikan edistämissäätiö TES through Foundations' Post Doc Pool, Finland.

REFERENCES

Babu, K.P., P.M. Mohite, and C.S. Updahyay. 2018. "Development of an RVE and its stiffness predictions based on mathematical homogenization theory for short fibre composites." International Journal of Solids and Structures 130-131: 80-104.

Bargmann, S., B. Klusemann, J. Markmann, J.E. Schnabel, K. Schneider, C. Soyarslan, and J. Wilmers. 2018. "Generation of 3D representative volume elements for heterogeneous materials: A review." Progress in Materials Science 96: 322–384.

Cerquaglia, M.L., G. Deliége, R. Boman, L. Papeleux, and J.P. Ponthot. 2017. "Reprint of: The particle finite element method for the numerical simulation of bird strike." International Journal of Impact Engineering 72-84.

Duval, L., M. Moreaud, C. Couprie, D. Jeulin, H. Talbot, and J. Angulo. 2014. "Image processing for materials characterization: Issues, challenges and opportunities." 2014 IEEE International Conference on Image Processing (ICIP). Paris.

Edelsbrunner, H. 1995. "Smooth surfaces for multi-scale shape representation." In Foundations of Software Technology and Theoretical Computer Science, 391-412. Berlin, Heidelberg: Springer.

Edelsbrunner, H., D. Kirkpatrick, and R. Seidel. 1983. "On the shape of a set of points in the plane." IEEE Transactions on Information Theory 29 (4): 551 - 559.

Evans, J.W. 1993. "Random and cooperative sequential adsorption." Reviews of Modern Physics 65 (1281).

Geers, M.G.D., V.G. Kouznetsova, and W.A.M. Brekelmans. 2010. "Multi-scale computational homogenization: Trends and challenges." Journal of Computational and Applied Mathematics 2175-2182.

Halpin, J.C. 1969. Effects of Environmental Factors on Composite. Ohio: AFML-TR-67-423.

Hashin, Z., and S. Shtrikman. 1963. "A Variational Approach to the Elastic Behavior of Multiphase Materials." Journal of the Mechanics and Physics of Solids 11 (2): 127-140.

Hernández, J.A., J. Oliver, A.E. Huespe, M.A. Caicedo, and J.C. Cante. 2014. "High-performance model reduction techniques in computational multiscale homogenization." Computer Methods in Applied Mechanics and Engineering 276: 149-189.

Hibbitt, Karlsson, and Sorensen. 1992. ABAQUS: Theory Manual. Providence, R.I.: Hibbitt, Karlsson & Sorensen.

Hollister, S.J., and N. Kikuchi. 1994. "Homogenization Theory and Digital Imaging: A Basis for Studying the Mechanics and Design Principles of Bone Tissue." Biotechnology and Bioengineering, Vol. 43: 586-596.

Huang, X., and B. Wei. 2010. "Mineral Particle Image Processing and Parameter Extracting." International Conference on Logistics Engineering and Intelligent Transportation System. Wuhan.

Hung, M.S., and W.O. Rom. 1980. "Solving the Assignment Problem by Relaxation." Operations Research 28 (4): 969-982.

Karakoc, A. 2018. "Sensitivity analysis on the effective stiffness properties of 3-D orthotropic honeycomb cores." International Journal for Computational Methods in Engineering Science and Mechanics 19 (1): 22-30.

Karakoc, A, and E Taciroglu. 2017. "Optimal automated path planning for infinitesimal and real-sized particle assemblies." AIMS Materials Science 4 (4): 847-855.

Karakoc, A., E. Hiltunen, and J. Paltakari. 2017. "Geometrical and spatial effects on fiber network connectivity." Composite Structures 168: 335-344.

Karakoç, A., P. Tukiainen, J. Freund, and M. Hughes. 2013. "Experiments on the effective compliance in the radial–tangential plane of Norway spruce." Composite Structures 102: 287-293.

Kushnevsky, V., O. Morachkovsky, and H. Altenbach. 1998. "Identification of effective properties of particle reinforced composite materials." Computational Mechanics 317-325.

Larsson, F., K. Runesson, S. Saroukhani, and R. Vafadari. 2011. "Computational homogenization based on a weak format of micro-periodicity for RVE-problems." Comput. Methods Appl. Mech. Eng. 200: 11-26.

Legrain, G., P. Cartraud, I. Perreard, and N. Moes. 2011. "An X- FEM and level set computational approach for image- based modelling: Application to homogenization." International Journal for Numerical Methods in Engineering 86 (7): 915-934.

Lian, W.D., G. Legrain, and P. Cartraud. 2013. "Image-based computational homogenization and localization: comparison between X-FEM/levelset and voxel-based approaches." Computational Mechanics 51 (3): 279-293.

Lopez, E., E. Abisset-Chavanne, C. Ghnatios, S. Comas-Cardona, C. Binetruy, and F. Chinesta. 2014. "Towards image-based homogenization by combining scanning techniques and reduced order modelling." ECCM-16TH European Conference on Composite Materials. Seville, Spain.

Nazar, A.M., F.A. Silva, and J.J. Ammann. 1996. "Image processing for particle characterization." Materials Characterization 36 (4-5): 165-173.

Nguyen, V.D., and L. Noels. 2014. "Computational homogenization of cellular materials." International Journal of Solids and Structures 51 (11-12): 2183-2203.

Nguyen, V.D., E. Béchet, C. Geuzaine, and L. Noels. 2012. "Imposing periodic boundary condition on arbitrary meshes by polynomial interpolation." Computational Materials Science 55: 390-406.

Ren, W., Z. Yang, R. Sharma, C. Zhang, and P.J. Withers. 2015. "Two-dimensional X-ray CT image based meso-scale fracture modelling of concrete." Engineering Fracture Mechanics 133: 24-39.

Rendl, F. 1988. "On the Euclidean assignment problem." Journal of Computational and Applied Mathematics 23 (3): 257-265.

Segurado, J., and J. Llorca. 2002. "A numerical approximation to the elastic properties of sphere-reinforced composites." Journal of the Mechanics and Physics of Solids 2107-2121.

Sjolund, J., A. Karakoc, and J. Freund. 2014. "Accuracy of regular wood cell structure model." Mechanics of Materials 76: 35-44.

Soden, P.D., M.J. Hinton, and A.S. Kaddour. 1998. "Lamina properties, lay-up configurations and loading conditions for a range of fibre-reinforced composite laminates." Compos. Sci. Technol. 58 (7): 1011-1022.

Takano, N., M. Zako, F. Kubo, and K. Kimura. 2003. "Microstructure-based stress analysis and evaluation for porous ceramics by homogenization method with digital image-based modeling." International Journal of Solids and Structures 40 (5): 1225-1242.

Terada, K., T. Miura, and N. Kikuchi. 1997. "Digital image-based modeling applied to the homogenization analysis of composite materials." Computational Mechanics 20: 331-346.

Tyrus, J.M., M. Gosz, and E. DeSantiago. 2007. "A local finite element implementation for imposing periodic boundary conditions on composite micromechanical models." Int. J. Solids Struct. 44 (9): 2972–2989.

Yuan, Z., and J. Fish. 2008. "Toward realization of computational homogenization in practice." Int. J. Numer. Methods Eng. 73 (3): 361-380.

Figure 1. *Various engineering materials at their material scales and the illustrations of their reconstructed microstructures as representative volume elements (RVEs): (a) closed cell porous material, (b) particle reinforced composite, (c) fiber reinforced composite, (d) nonwoven material.*

Figure 2. *Flow chart for the present algorithm and schematic illustration of the boundary and control node matching on a representative volume element RVE based on the proposed method. The term* $\partial\omega$ *represents the boundaries of the RVE and* $\partial\Gamma$ *represents the boundaries of rectangular prism bounding the RVE. It is noteworthy that boundaries comprise of vertices, edges and surfaces.*

Figure 3. *Illustration of the rectangular prism bounding the RVE and control node sets (q) on its boundaries (*$\partial\Gamma$*). The symbols on the right-hand sides of the nodes show the matching sets for the periodicity.*

Figure 4: *Details of the control node reduction. R refers to circumradius of the element.*

Figure 5. *Strain driven homogenization with imposed macroscopic strain* $\mathbf{e}^{\mathrm{M}}$ *and computed stress* $\mathbf{s}^{\mathrm{M}}$. *Here,* $\mathbf{\Omega}$ *and* $\partial\mathbf{\Omega}$ *represent the volume and boundary of continuum, and* Γ *and* $\partial\Gamma$ *represent the volume and boundary of the rectangular prism that bounds the RVE.*

Figure 6. *Mesh size investigations: (a) coarsest mesh (I), optimum mesh comprising the CPU time and properties (II), finest mesh (III), (b) effect of mesh size on the convergence of effective elastic properties and CPU time.*

Figure 7. *Control node investigations: (a) representative volume element RVE with 152 control nodes (I), 2402 nodes (II), 3628 nodes (III), (b) effect of number of control nodes on the effective elastic properties and CPU time.*

Figure 8. *Deformation modes of the closed cell porous material: (a) top and bottom isometric views, (b) uniaxial deformation modes, (c) shear deformation modes. A deformation scale factor of 10 was used for better illustration.*

Figure 9. *Deformation modes of spherical particle reinforced composite: (a) isometric view, (b) generated arbitrary mesh on the RVE boundaries, (c) uniaxial deformation modes, (d) shear deformation modes. A deformation scale factor of 10 was used for better illustration.*

Figure 10. *Deformation modes of short fiber reinforced composite: (a) isometric view, (b) generated arbitrary mesh on the RVE boundaries, (c) uniaxial deformation modes, (d) shear deformation modes. A deformation scale factor of 5 was used for better illustration.*

Table 1. *Effect of void volume fraction V_f on the effective elastic properties of closed cell porous materials. HS refers to Hashin-Shtrikman. Perc. Diff. refers to the percentile difference between the mean values of the simulations and ones from Hashin-Shtrikman equations.*

V_f (%)		E_{c11} (MPa)	E_{c22} (MPa)	E_{c33} (MPa)	G_{c12} (MPa)	G_{c13} (MPa)	G_{c23} (MPa)	ν_{c12}	ν_{c13}	ν_{c23}
10	RVE 1	2456.4	2420.6	2444.8	900.9	904.5	903.3	0.35	0.35	0.35
	RVE 2	2463.3	2430.7	2477.7	904.1	903.9	903.3	0.35	0.35	0.35
	RVE 3	2497.5	2397.0	2451.5	900.3	906.9	896.6	0.36	0.36	0.35
	Mean	2472.4	2416.1	2458.0	901.8	905.1	901.1	0.35	0.35	0.35
	Std Dev	22.0	17.3	17.4	2.0	1.6	3.9	0.02	0.02	0.01
	HS-Lower	2457.6	2457.6	2457.6	903.9	903.9	903.9	0.36	0.36	0.36
	Perc. Diff. (%)	0.6	1.7	0.04	0.2	0.1	0.3	1.4	1.7	3.3
15	RVE 1	2242.5	2243.5	2251.7	823.6	829.7	828.5	0.34	0.35	0.34
	RVE 2	2279.0	2280.2	2243.3	844.1	840.1	833.3	0.35	0.35	0.35
	RVE 3	2281.6	2267.7	2296.5	847.1	850.9	845.3	0.35	0.35	0.34
	Mean	2267.7	2263.8	2263.8	838.3	840.3	835.7	0.35	0.35	0.34
	Std Dev	21.9	18.7	28.6	12.8	10.6	8.7	0.00	0.00	0.00
	HS-Lower	2212.4	2212.4	2212.4	819.4	819.4	819.4	0.35	0.35	0.35
	Perc. Diff. (%)	2.4	2.3	2.3	2.3	2.5	2.0	1.0	0.7	1.9
20	RVE 1	2062.3	2029.5	2052.0	759.0	763.2	759.7	0.34	0.34	0.34
	RVE 2	2059.8	2010.8	2049.2	753.7	748.7	751.1	0.34	0.34	0.34
	RVE 3	1989.6	1930.0	1980.4	738.0	744.3	737.0	0.34	0.34	0.33
	Mean	2037.2	1990.1	2027.2	750.3	752.1	749.3	0.34	0.34	0.33
	Std Dev	41.3	52.9	40.5	10.9	9.9	11.5	0.00	0.00	0.00
	HS-Lower	2004.7	2004.7	2004.7	746.8	746.8	746.8	0.34	0.34	0.34
	Perc. Diff. (%)	1.6	0.7	1.1	0.5	0.7	0.3	0.1	1.0	2.3
25	RVE 1	1871.3	1848.7	1818.4	679.0	683.1	685.4	0.33	0.33	0.33
	RVE 2	1903.9	1841.6	1869.5	709.3	707.1	700.6	0.34	0.34	0.33
	RVE 3	1800.8	1795.5	1763.3	673.2	665.3	664.4	0.33	0.33	0.33
	Mean	1858.7	1828.6	1817.1	687.2	685.2	683.5	0.33	0.33	0.33
	Std Dev	52.7	28.9	53.1	19.4	21.0	18.2	0.01	0.00	0.00
	HS-Lower	1805.1	1805.1	1805.1	676.3	676.3	676.3	0.33	0.33	0.33
	Perc. Diff. (%)	2.9	1.3	0.7	1.6	1.3	1.1	0.8	0.6	1.4
28	RVE 1	1793.9	1703.2	1735.5	656.5	653.8	650.5	0.34	0.33	0.32
	RVE 2	1720.0	1724.8	1709.2	648.8	644.1	643.8	0.33	0.33	0.33
	RVE 3	1810.8	1783.4	1776.8	675.3	675.3	666.2	0.33	0.33	0.32
	Mean	1774.9	1737.1	1740.5	660.2	657.7	653.5	0.33	0.33	0.32
	Std Dev	48.3	41.5	34.1	13.6	15.9	11.5	0.01	0.00	0.00
	HS-Lower	1729.6	1729.6	1729.6	649.4	649.4	649.4	0.33	0.33	0.33
	Perc. Diff. (%)	2.5	0.4	0.6	1.6	1.3	0.6	0.2	0.2	2.1

Table 2. *Effect of particle volume fraction on the effective elastic properties of spherical particle reinforced composites. HS refers to Hashin-Shtrikman. Perc. Diff. refers to the percentile difference between the mean values of the simulations and ones from Hashin-Shtrikman equations.*

V_f (%)		E_{c11} (MPa)	E_{c22} (MPa)	E_{c33} (MPa)	G_{c12} (MPa)	G_{c13} (MPa)	G_{c23} (MPa)	ν_{c12}	ν_{c13}	ν_{c23}
10	RVE 1	3753.2	3733.3	3729.3	1366.4	1361.9	1357.4	0.36	0.37	0.37
	RVE 2	3809.2	3750.5	3772.8	1371.7	1377.3	1369.6	0.37	0.36	0.37
	RVE 3	3775.3	3798.8	3792.7	1384.0	1392.8	1378.2	0.36	0.37	0.36
	Mean	3779.2	3760.8	3764.9	1374.0	1377.3	1368.4	0.36	0.37	0.37
	Std Dev	28.2	34.0	32.4	9.0	15.4	10.5	0.00	0.00	0.00
	HS-Lower	3648.6	3648.6	3648.6	1331.1	1331.1	1331.1	0.37	0.37	0.37
	Perc. Diff. (%)	3.5	3.0	3.1	3.1	3.4	2.7	1.6	1.2	1.5
15	RVE 1	4266.5	4242.9	4265.3	1549.8	1543.1	1568.5	0.36	0.36	0.36
	RVE 2	4326.9	4265.3	4306.5	1540.0	1557.4	1535.5	0.36	0.36	0.36
	RVE 3	4168.1	4148.4	4149.6	1497.1	1512.1	1506.9	0.35	0.36	0.36
	Mean	4253.8	4218.8	4240.5	1529.0	1537.5	1537.0	0.36	0.36	0.36
	Std Dev	80.1	62.0	81.4	28.0	23.2	30.8	0.00	0.00	0.00
	HS-Lower	4023.3	4023.3	4023.3	1472.8	1472.8	1472.8	0.37	0.37	0.37
	Perc. Diff. (%)	5.4	4.6	5.1	3.7	4.2	4.2	2.7	2.3	2.0
20	RVE 1	4853.3	4873.5	4931.8	1732.7	1717.8	1776.3	0.35	0.34	0.35
	RVE 2	4920.3	4944.5	4940.9	1760.5	1794.8	1806.8	0.34	0.35	0.35
	RVE 3	5003.4	4983.4	5055.6	1781.8	1829.1	1825.7	0.34	0.34	0.35
	Mean	4925.7	4933.8	4976.1	1758.4	1780.5	1802.9	0.34	0.35	0.35
	Std Dev	75.2	55.7	69.0	24.6	57.0	24.9	0.00	0.01	0.00
	HS-Lower	4439.1	4439.1	4439.1	1630.4	1630.4	1630.4	0.36	0.36	0.36
	Perc. Diff. (%)	9.9	10.0	10.8	7.3	8.4	9.6	5.3	4.6	4.0
25	RVE 1	5630.5	5705.4	6191.6	2057.0	2100.9	2130.1	0.35	0.31	0.31
	RVE 2	5683.1	5820.2	5631.5	2087.1	2019.4	2055.3	0.33	0.34	0.34
	RVE 3	5776.8	5966.4	5851.2	2117.7	2116.1	2216.0	0.32	0.34	0.34
	Mean	5696.8	5830.6	5891.5	2087.2	2078.8	2133.8	0.33	0.33	0.33
	Std Dev	74.1	130.8	282.2	30.4	52.0	80.4	0.01	0.02	0.02
	HS-Lower	4903.3	4903.3	4903.3	1806.9	1806.9	1806.9	0.36	0.36	0.36
	Perc. Diff. (%)	13.9	15.9	16.8	13.4	13.1	15.3	7.1	8.1	8.8
28	RVE 1	6201.6	5985.4	6131.5	2148.5	2247.3	2129.8	0.33	0.34	0.33
	RVE 2	6567.9	6643.9	6631.7	2391.3	2390.8	2438.7	0.32	0.33	0.32
	RVE 3	6341.2	6167.5	6338.8	2252.2	2218.1	2209.2	0.34	0.32	0.32
	Mean	6370.2	6265.6	6367.3	2264.0	2285.4	2259.3	0.33	0.33	0.32
	Std Dev	184.9	340.1	251.3	121.8	92.4	160.4	0.01	0.01	0.00
	HS-Lower	5251.3	5251.3	5251.3	1939.6	1939.6	1939.6	0.35	0.35	0.35
	Perc. Diff. (%)	17.6	16.2	17.5	14.3	15.1	14.2	7.1	8.0	9.1

Table 3. *Effect of fiber volume fraction on the effective elastic properties of fibre reinforced composites. Perc. Diff. refers to the percentile difference between the values of the simulations and ones from Halpin-Tsai equations.*

V_f (%)		E_{c11} (MPa)	E_{c22} (MPa)	E_{c33} (MPa)	G_{c12} (MPa)	G_{c13} (MPa)	G_{c23} (MPa)	ν_{c12}	ν_{c13}	ν_{c23}
16	RVE	8880.4	5052.5	5010.7	1993.3	2089.7	1862.9	0.32	0.31	0.38
	Halpin-Tsai	10205.2	5423.9	5423.9	2025.5	2025.5	1914.5	0.32	0.32	-
	Perc. Diff. (%)	13.0	6.8	7.6	1.6	3.2	2.7	0.5	3.9	-
17	RVE	10337.9	5246.6	5156.3	2089.9	2127.6	1874.1	0.31	0.31	0.38
	Halpin-Tsai	10872.0	5549.4	5549.4	2074.8	2074.8	1950.6	0.32	0.32	-
	Perc. Diff. (%)	4.9	5.5	7.1	0.7	2.5	3.9	1.9	2.3	-
19	RVE	10403.0	5292.2	5249.6	2104.2	2221.3	1921.5	0.31	0.31	0.38
	Halpin-Tsai	11499.3	5665.8	5665.8	2121.0	2121.0	1984.2	0.32	0.32	-
	Perc. Diff. (%)	9.5	6.6	7.3	0.8	4.7	3.2	0.6	2.8	-
20	RVE	11415.6	5361.2	5397.6	2151.7	2362.8	1954.3	0.32	0.30	0.38
	Halpin-Tsai	12142.2	5783.3	5783.3	2168.0	2168.0	2018.2	0.31	0.31	-
	Perc. Diff. (%)	6.0	7.3	6.7	0.8	9.0	3.2	1.7	4.3	-
23	RVE	12390.0	5585.9	5552.8	2255.9	2465.6	2032.9	0.31	0.30	0.38
	Halpin-Tsai	13747.8	6069.6	6069.6	2284.3	2284.3	2101.4	0.31	0.31	-
	Perc. Diff. (%)	9.9	8.0	8.5	1.2	7.9	3.3	1.0	3.0	-
25	RVE	13999.0	5771.3	5782.4	2410.3	2650.3	2100.3	0.31	0.30	0.37
	Halpin-Tsai	15049.1	6294.2	6294.2	2377.3	2377.3	2167.0	0.30	0.30	-
	Perc. Diff. (%)	7.0	8.3	8.1	1.4	11.5	3.1	1.5	2.4	-
27	RVE	14391.6	5971.6	5927.4	2477.8	2643.9	2184.2	0.30	0.29	0.37
	Halpin-Tsai	16291.0	6502.7	6502.7	2465.1	2465.1	2228.1	0.30	0.30	-
	Perc. Diff. (%)	11.7	8.2	8.8	0.5	7.3	2.0	2.0	3.1	-
29	RVE	16757.7	6090.6	6164.2	2569.6	2887.7	2230.6	0.30	0.29	0.37
	Halpin-Tsai	17523.1	6704.1	6704.1	2551.2	2551.2	2287.5	0.30	0.30	-
	Perc. Diff. (%)	4.4	9.2	8.1	0.7	13.2	2.5	1.0	2.3	-
30	RVE	15688.3	6169.1	6228.0	2565.5	2885.9	2221.2	0.30	0.29	0.36
	Halpin-Tsai	17851.9	6757.0	6757.0	2574.0	2574.0	2303.1	0.30	0.30	-
	Perc. Diff. (%)	12.1	8.7	7.8	0.3	12.1	3.6	0.7	3.3	-
33	RVE	19945.3	6418.7	6484.8	2755.6	3023.3	2340.0	0.30	0.28	0.37
	Halpin-Tsai	20171.7	7119.7	7119.7	2733.1	2733.1	2410.7	0.29	0.29	-
	Perc. Diff. (%)	1.1	9.8	8.9	0.8	10.6	2.9	3.4	5.1	-

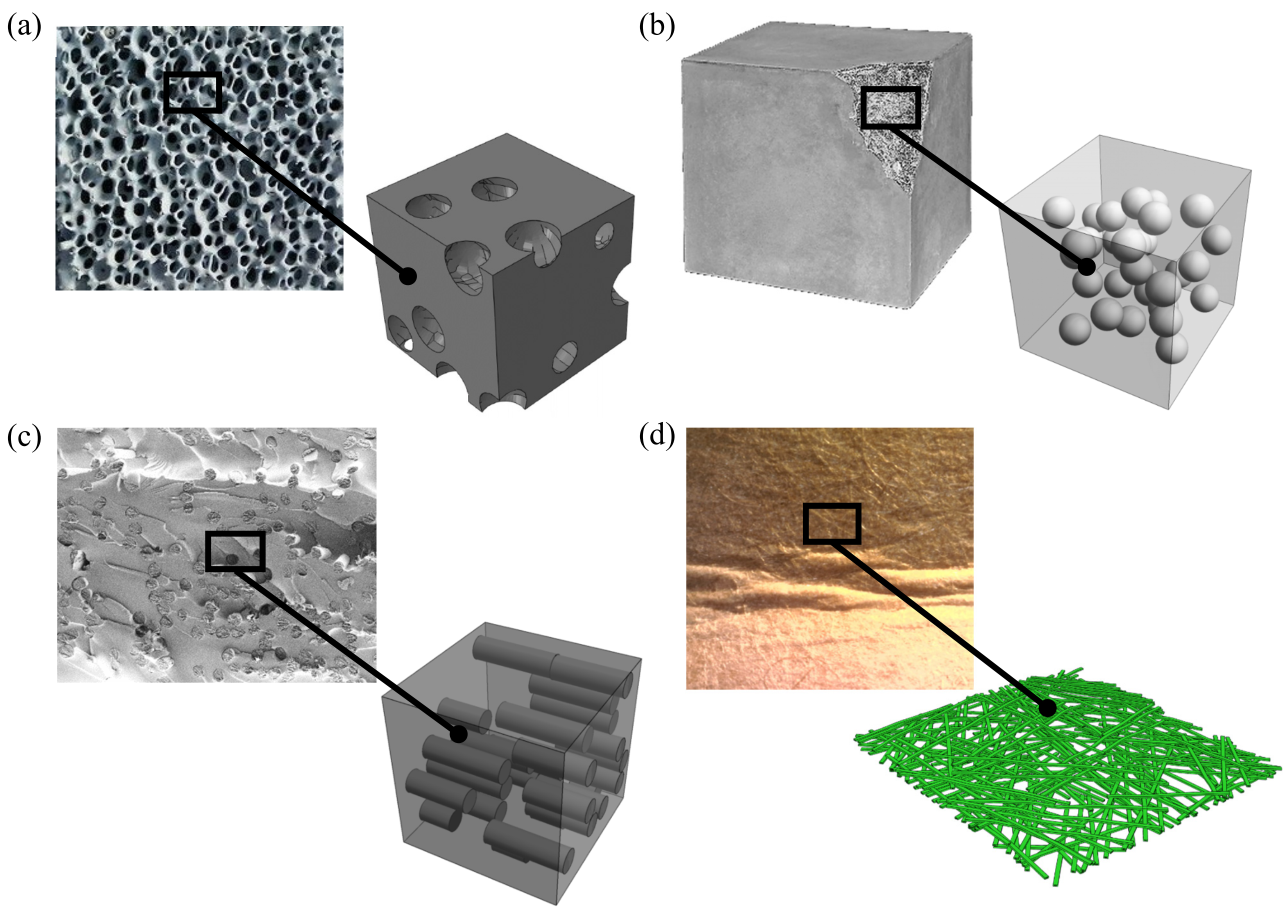
(a)
(b)
(c)
(d)

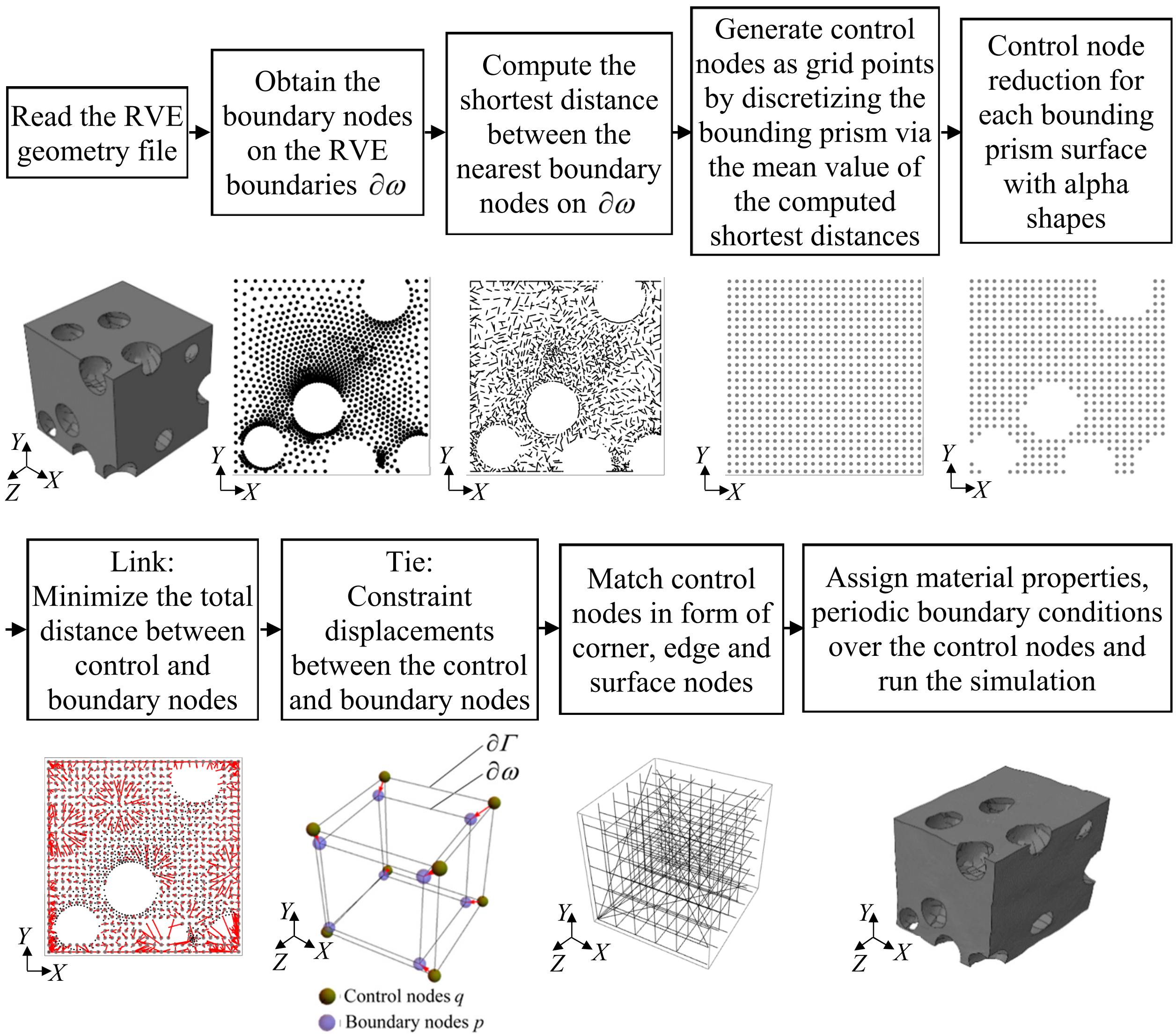

Read the RVE geometry file
Obtain the boundary nodes on the RVE boundaries $\partial\omega$
Compute the shortest distance between the nearest boundary nodes on $\partial\omega$
Generate control nodes as grid points by discretizing the bounding prism via the mean value of the computed shortest distances
Control node reduction for each bounding prism surface with alpha shapes
Link: Minimize the total distance between control and boundary nodes
Tie: Constraint displacements between the control and boundary nodes
Match control nodes in form of corner, edge and surface nodes
Assign material properties, periodic boundary conditions over the control nodes and run the simulation
$\partial\Gamma$
$\partial\omega$
Control nodes q
Boundary nodes p

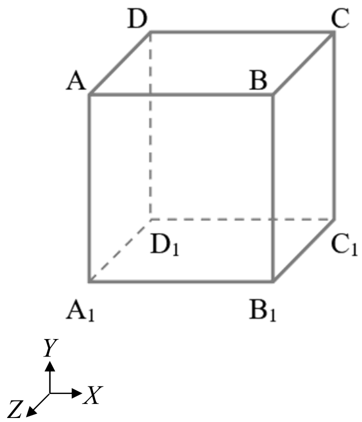

Corner nodes		Edge nodes		Surface nodes	
Node at point A	□	Nodes on edge AB	●	Nodes on surface ABCD	♦
Node at point B	□	Nodes on edge BC	○	Nodes on surface $A_1B_1C_1D_1$	♦
Node at point C	□	Nodes on edge DC	●	Nodes on surface AA_1D_1D	◘
Node at point D	□	Nodes on edge AD	○	Nodes on surface BB_1C_1C	◘
Node at point A_1	□	Nodes on edge A_1B_1	●	Nodes on surface DD_1C_1C	⌂
Node at point B_1	□	Nodes on edge B_1C_1	○	Nodes on surface AA_1B_1B	⌂
Node at point C_1	□	Nodes on edge D_1 C_1	●		
Node at point D_1	□	Nodes on edge A_1 D_1	○		
		Nodes on edge A_1A	◊		
		Nodes on edge B_1B	◊		
		Nodes on edge C_1C	◊		
		Nodes on edge D_1D	◊		

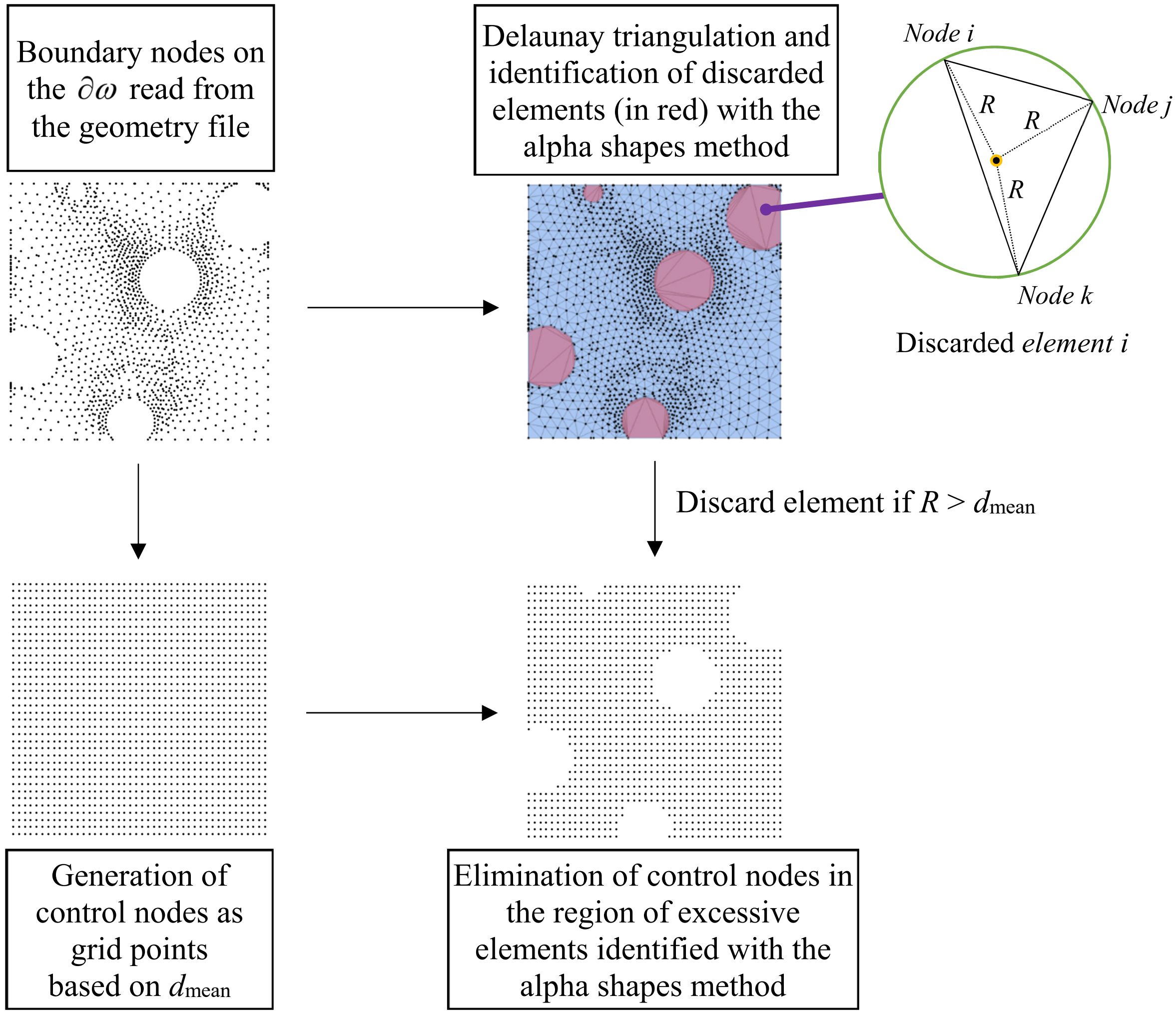

Boundary nodes on the $\partial\omega$ read from the geometry file
Delaunay triangulation and identification of discarded elements (in red) with the alpha shapes method
Node i
Node j
Node k
R
R
R
Discarded element i
Discard element if $R > d_{\mathrm{mean}}$
Generation of control nodes as grid points based on d_{mean}
Elimination of control nodes in the region of excessive elements identified with the alpha shapes method

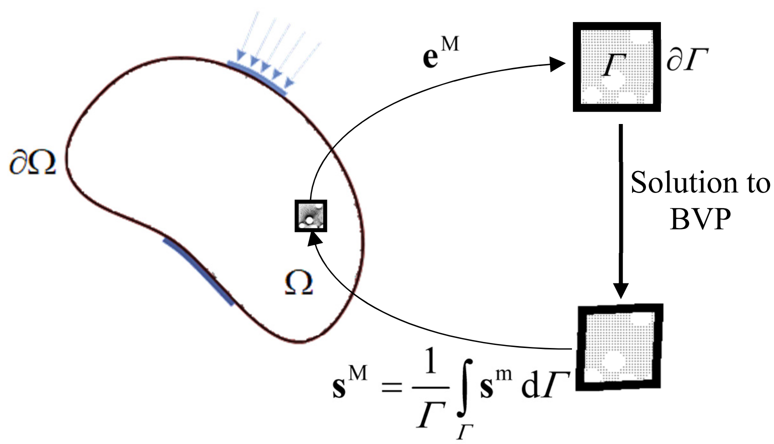
$\mathbf{e}^{\mathrm{M}}$
$\mathit{\Gamma}$
$\partial\mathit{\Gamma}$
$\partial\Omega$
Solution to BVP
Ω
$\mathbf{s}^{\mathrm{M}} = \frac{1}{\mathit{\Gamma}}\int_{\mathit{\Gamma}} \mathbf{s}^{\mathrm{m}}\, \mathrm{d}\mathit{\Gamma}$

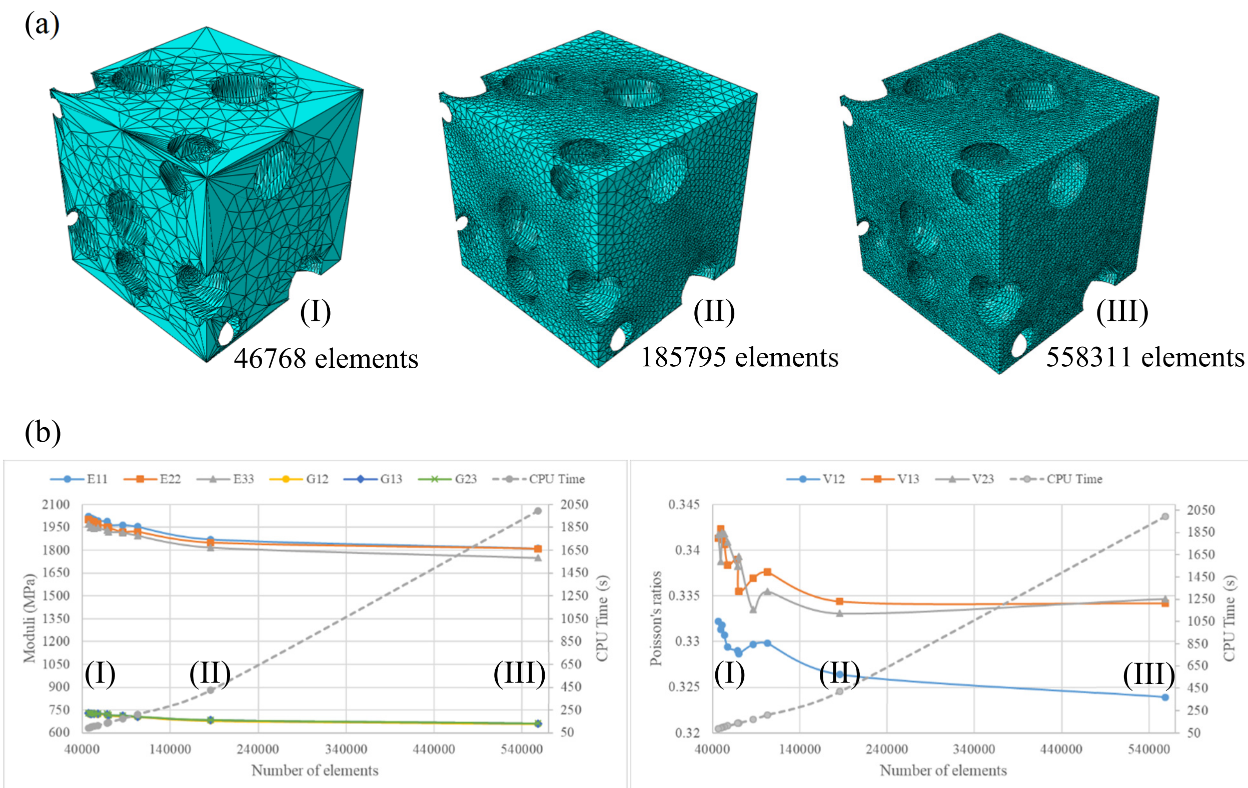

(a)
(I)
46768 elements
(II)
185795 elements
(III)
558311 elements
(b)
E11
E22
E33
G12
G13
G23
CPU Time
Moduli (MPa)
CPU Time (s)
Number of elements
(I)
(II)
(III)
V12
V13
V23
CPU Time
Poisson's ratios
CPU Time (s)
Number of elements
(I)
(II)
(III)

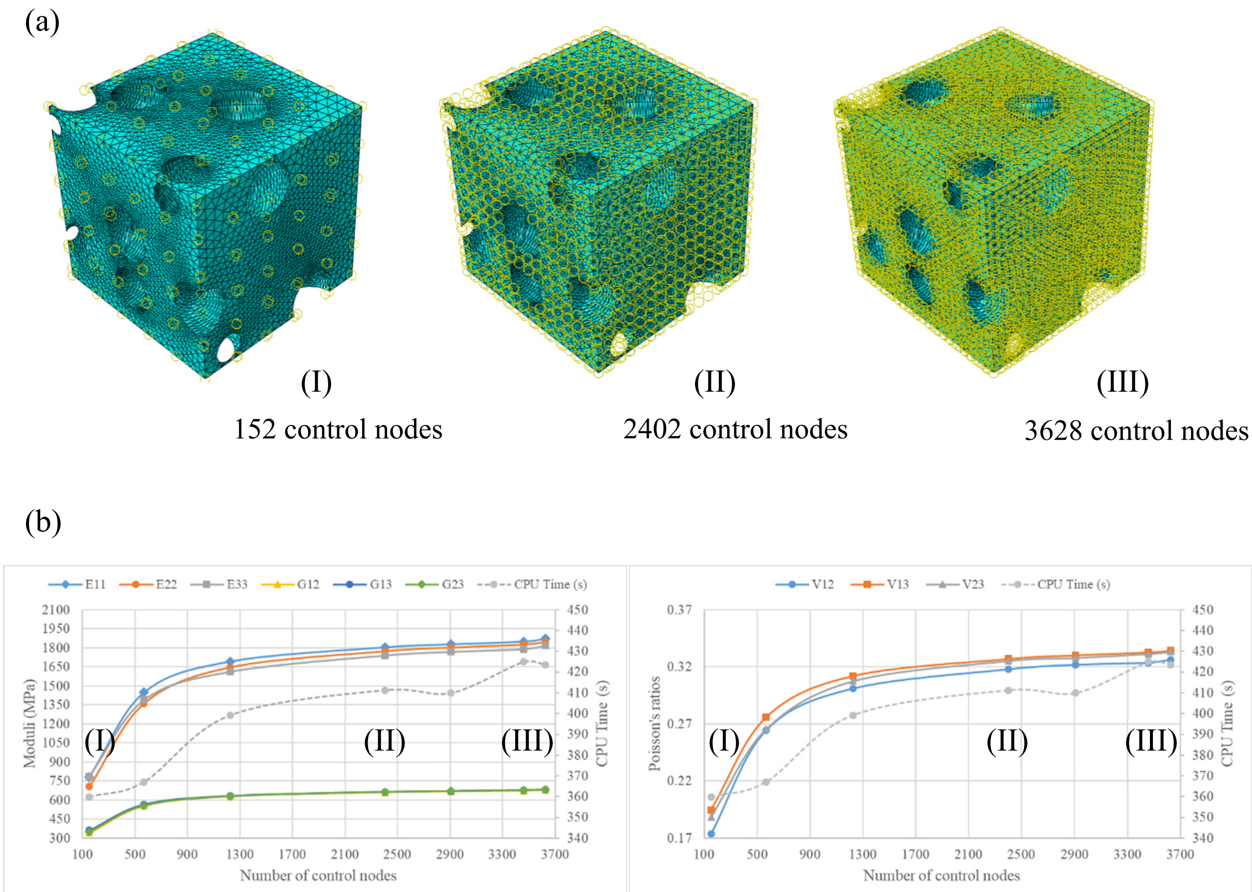
(a)
(I)
152 control nodes
(II)
2402 control nodes
(III)
3628 control nodes
(b)
E11
E22
E33
G12
G13
G23
CPU Time (s)
Moduli (MPa)
CPU Time (s)
Number of control nodes
(I)
(II)
(III)
V12
V13
V23
CPU Time (s)
Poisson's ratios
CPU Time (s)
Number of control nodes
(I)
(II)
(III)

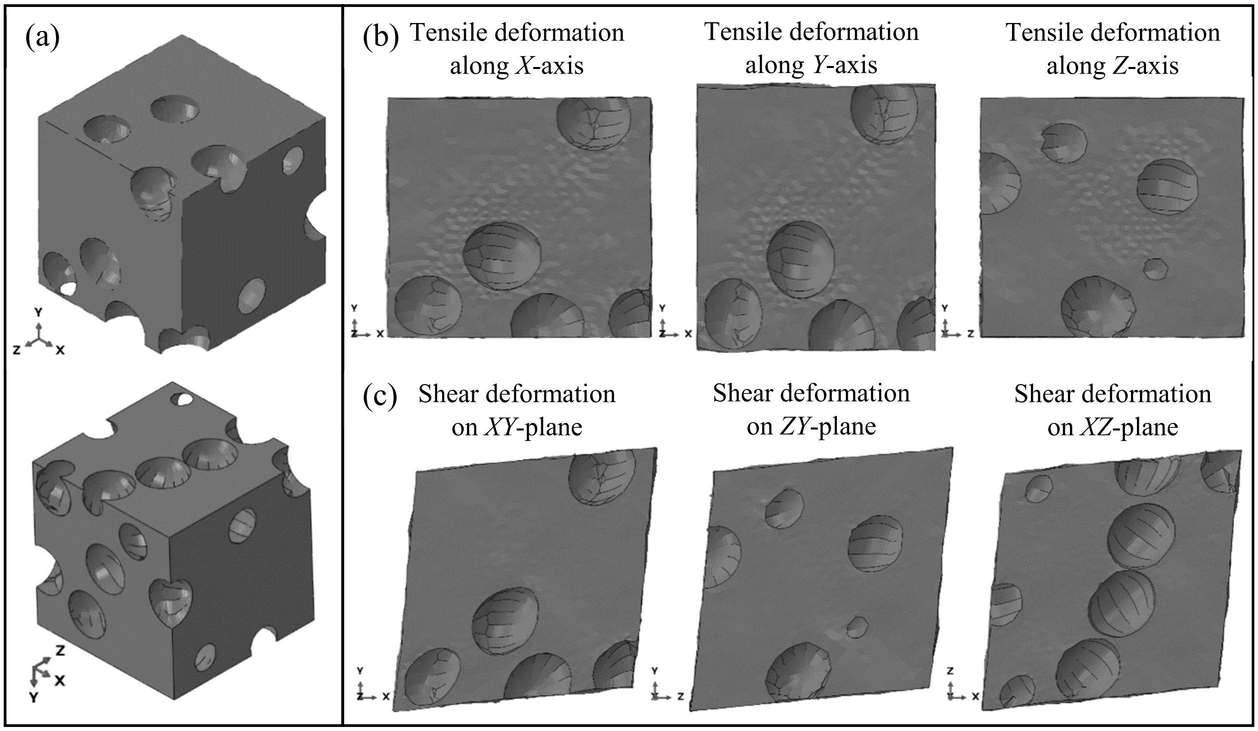
(a)
(b) Tensile deformation along X-axis
Tensile deformation along Y-axis
Tensile deformation along Z-axis
(c) Shear deformation on XY-plane
Shear deformation on ZY-plane
Shear deformation on XZ-plane
Y
Z
X

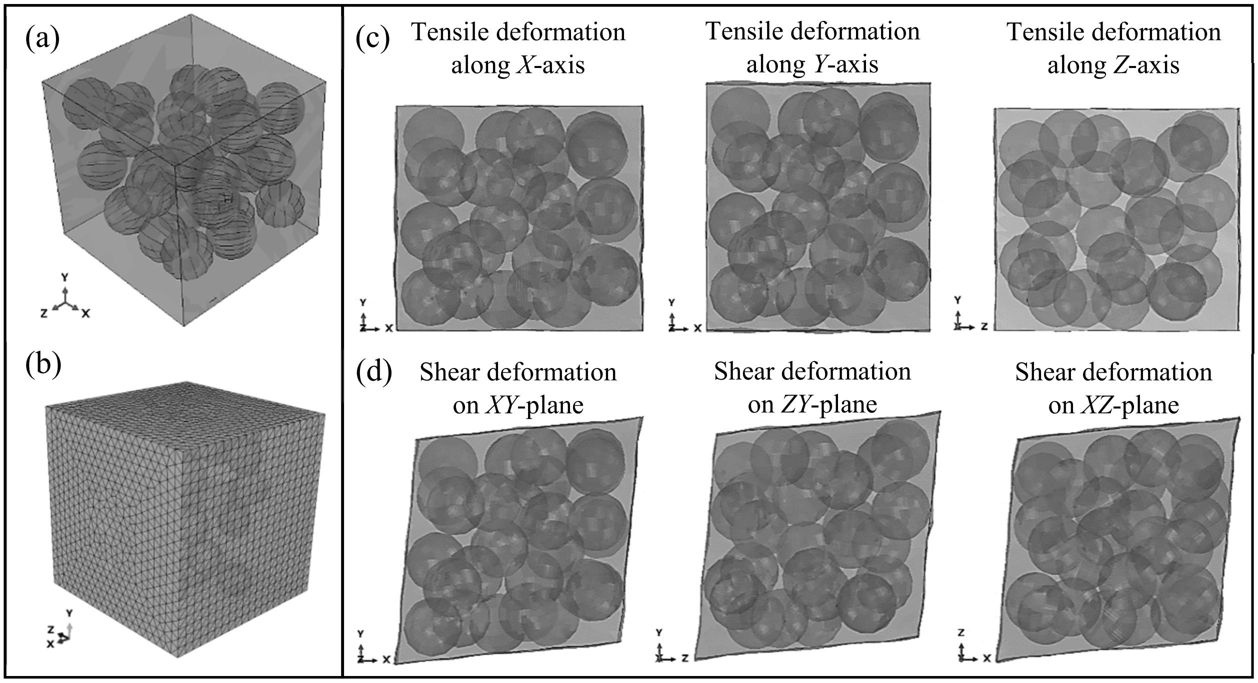
(a)
(b)
(c) Tensile deformation along X-axis
Tensile deformation along Y-axis
Tensile deformation along Z-axis
(d) Shear deformation on XY-plane
Shear deformation on ZY-plane
Shear deformation on XZ-plane

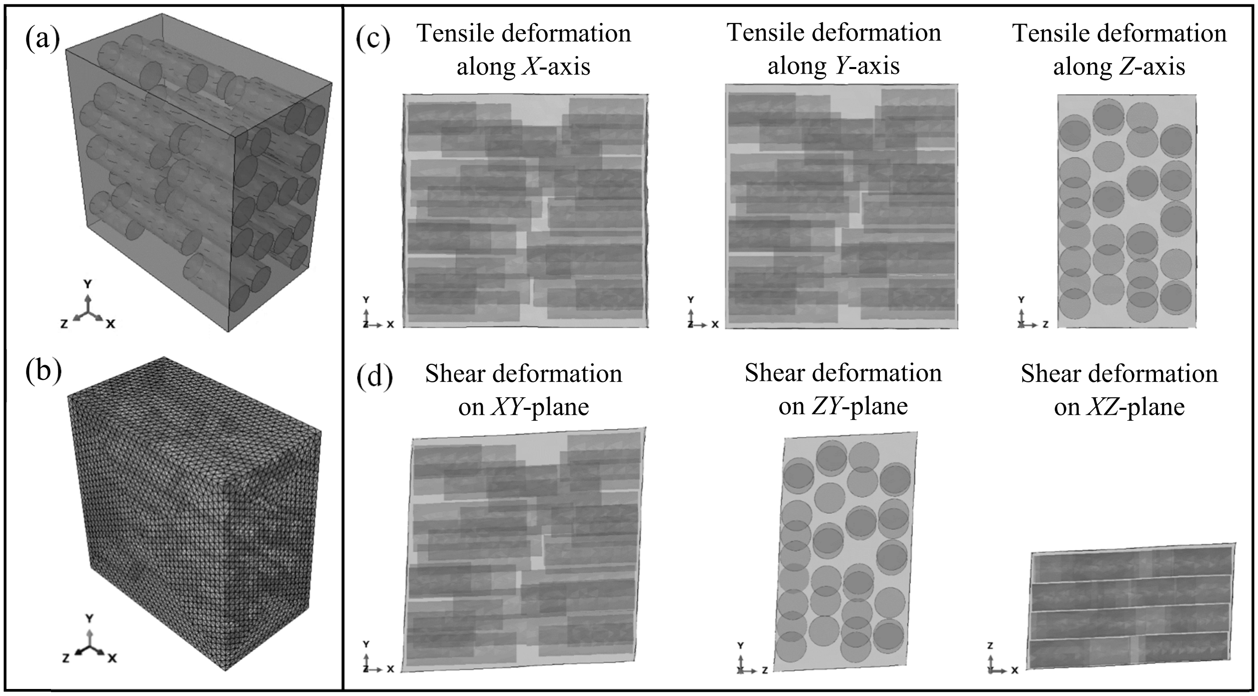
(a)
(b)
(c)
Tensile deformation along X-axis
Tensile deformation along Y-axis
Tensile deformation along Z-axis
(d)
Shear deformation on XY-plane
Shear deformation on ZY-plane
Shear deformation on XZ-plane